Part Two

Biomedical Applications and Microscopy

6

Advanced Digital Holographic Microscopy for Life Science Applications

Frank Dubois, Ahmed El Mallahi, Christophe Minetti and Catherine Yourassowsky
Microgravity Research Centre, Université Libre de Bruxelles, Belgium

6.1 Introduction

A *digital holographic microscope* (DHM) is a powerful tool for recording full interferometric information of objects. It provides the capability to record sequences of holograms of dynamic phenomena at high rates and with short exposure times. The analyses are based on the digital holographic refocusing of both the optical intensities and quantitative optical phase maps. In this chapter, we present the developments we have realized on these instrumentations and holographic information processing. Our instrumental developments are based on the use of optical illumination sources of reduced coherences in order to improve the optical quality of the both phase maps and intensities. Although the reduction of the spatial coherence is most significant with a transmission DHM, the reduction in temporal coherence is also relevant to reducing the noise with high scattering samples. In this way, we recently developed a microscope with multi-wavelength sources of both spatial and temporal reduced coherences enabling one-shot recording. The DHM configurations are detailed in Section 6.2. The processing of holograms has been developed in several applications. In Sections 6.3 and 6.4, they are illustrated in water monitoring and the study of dynamical behavior of red blood cells. Some concluding remarks are provided in Section 6.5.

6.2   DHM Configurations

6.2.1   *Phase Stepper DHM*

The first DHM we developed was a phase stepper configuration with a partially coherent source realized from a spatially filtered *light emitting diode* (LED) (Fig. 6.1) [1]. The partially coherent illumination improves the quality of the holographic recording by decreasing the coherent artifact noise. With this DHM, the image quality is excellent, even considering the intensities, and is comparable to those obtained with classical optical microscopes (Fig. 6.2). According to the extraction of the complex amplitude by phase stepping [2], the partially coherent illumination allows retaining the two major capabilities of the DHM: (1) refocusing of objects recorded out of focus; (2) performing quantitative phase contrast imaging, even in high-scattering media [3–6].

We mainly used this microscope configuration for adherent cell culture applications.

6.2.2   *Fast Off-Axis DHM*

With the phase stepper configuration, the angle between the reference and the object beams incident on the camera sensor is as small as possible. Therefore, the method requests the sequential recording of several interferometric images that limits acquisition speed due to the camera frame rate. It means that the object has to remain static during the complete acquisition that takes the time of recording several frames. To overcome this limitation, we developed an off-axis fast DHM [7] with a partial coherent source for which the phase map and intensity method are obtained from each recorded hologram thanks to the Fourier method (Fig. 6.3) [8,9].

In this configuration, an angle is introduced between the object beam and the reference beam in order to obtain spatial heterodyne fringes (off-axis configuration). With respect to the phase stepper configuration, the full one-shot recording of the holographic information is a decisive advantage in the analysis of rapidly varying phenomena. An example obtained with the DHM set up to perform time lapse on fresh water flux in micro-channels is shown by Fig. 6.4.
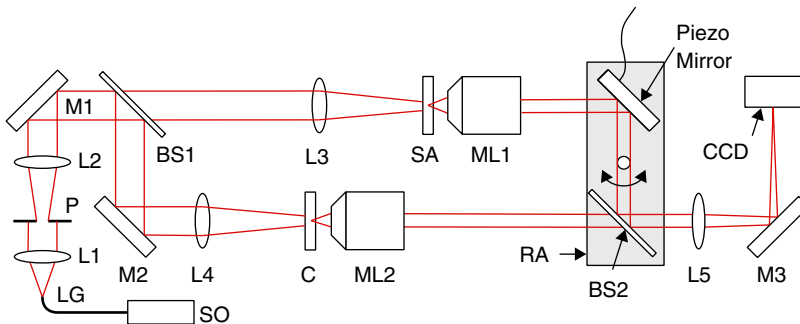

Figure 6.1   DHM microscope with LED illumination and phase stepper. SO: The LED module, LG: liquid light guide, L1–L5: Achromatic lenses, P: Aperture, M1–M3: Mirrors, BS1 and BS2: Beamsplitters, ML1, ML2: Microscope lenses, SA: Sample, C: Optical path compensator, RA: rotation assembly, CCD: camera, Piezo Mirror: mirror mounted on a piezoelectric transducer
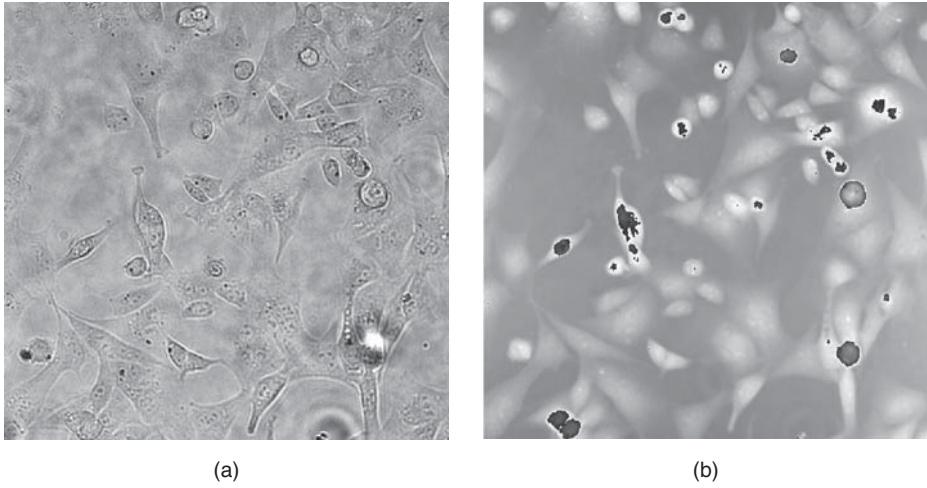
(a)   (b)

Figure 6.2 Adherent cell culture. (a) Intensity, (b) quantitative phase image obtained with the phase stepper DHM with LED illumination. FOV = $400 \times 400\,\mu$m. *Source*: Dubois *et al*. 2011. Reproduced with permission from Springer
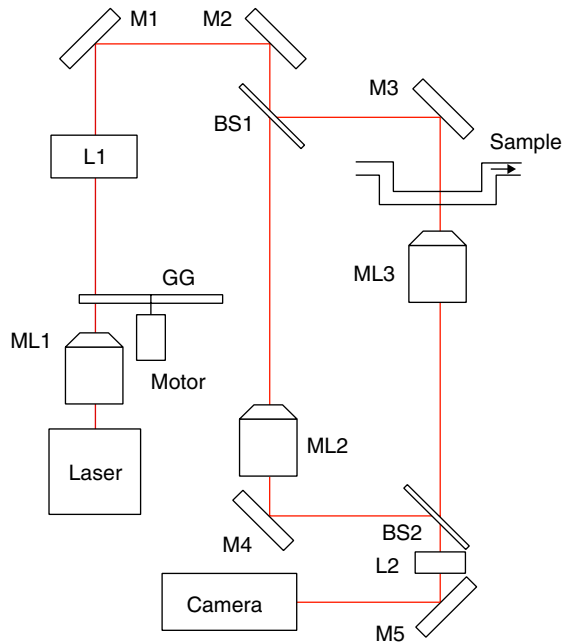

Figure 6.3 Fast DHM configuration with a reduced spatial coherence source created from a laser beam
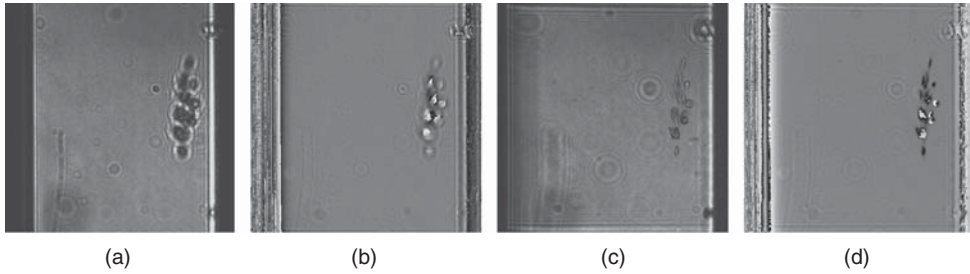
(a) (b) (c) (d)

Figure 6.4 An alga in a micro-channel. FOV $= 370 \times 370$ µm. (a) out of focus intensity image, (b) out of focus phase image, (c) refocused intensity image, (d) refocused phase image

Each particle or organism can be refocused and analyzed thanks to the quantitative phase contrast imaging capability, allowing a high throughput monitoring of fresh water. However, the off-axis configuration requests an optical source of high temporal coherence. Otherwise, the fringe modulation is not constant due to variable optical delays over the field of view between the object and reference beams. If the path length differences between the reference beam and the object beam become larger locally than the coherence length of the incident beam, no interference can be observed and the phase information is lost. This means that, with temporally partially coherent light, the difference between the path lengths at different positions in the recording plane can be sufficient to disrupt coherency, so interferences will only be observed in part of the recording plane in which the coherency is maintained.

As shown in the Fig. 6.3, the optical source of high temporal coherence with reduced partial spatial coherence can be obtained with a laser beam focused close to a moving ground glass. For a given position of the ground glass, the transmitted light through the sample is a speckle field. When the ground glass is moving, and assuming that the exposure time is long enough to obtain an averaging effect, this type of source is equivalent to a spatial partial coherent light with a spatial coherence width equal to the average speckle field. However, illumination fluctuations arise when short exposure times are requested. When very fast acquisition is required, it is difficult to achieve fast enough moving ground glass.

6.2.3 Color DHM

In order to overcome the limitation of the fast off-axis DHM described here previously, we developed a new DHM configuration, which enables the use of the off-axis configuration with a partial temporal and spatial coherent light beam. It is a significant improvement as it allows operation of the microscope in fast mode without the disadvantage of fluctuations resulting from the configuration with a laser. Moreover, this implementation enables the use of low cost sources such as LED and gives the possibility of simultaneously recording red-green-blue high quality holograms to provide full color digital holographic microscopy at very low noise levels [10]. In this new DHM configuration, the coherence plane of the reference light beam is not perpendicular to the propagation direction in the vicinity of the recording plane. This results in the ability of this light beam to interfere with object beam, whose coherence plane is perpendicular to the propagation direction, and to produce a fringe contrast independent of the position on the recording plane. This permits the recording of off-axis interfering fringes
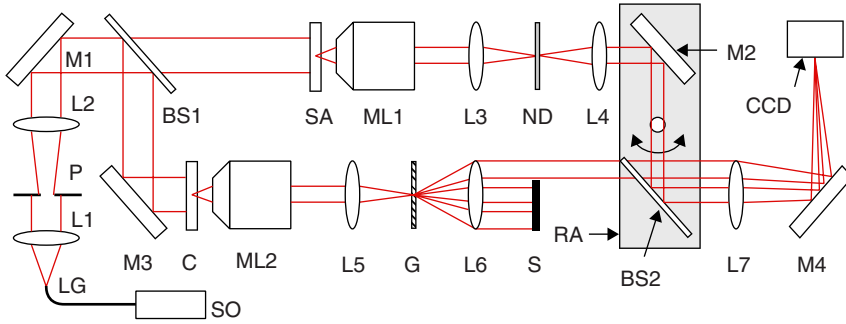
Figure 6.5 The optical setup. SO: The RGB LED module, LG: liquid light guide, L1–L7: Achromatic lenses, P: Aperture, M1–M4: Mirrors, BS1 and BS2: Beamsplitters, ML1, ML2: Microscope lenses, SA: Sample, C: Optical path compensator, G: Grating, S: Optical stop, RA: rotation assembly, CCD: Camera. ND: Neutral density filter to adjust the beam intensity ratio. *Source*: Dubois 2012. Reproduced with permission from the Optical Society

(spatially heterodyne fringes) even in the case of light with limited coherence length, such as the light produced by a LED, a gas discharge lamp. Those configurations take advantage of the particular properties of diffraction gratings for producing an off-axis reference beam without disrupting the temporal coherence of interfering beams in the recording plane. The transmission DHM configuration based on that concept is shown by Fig. 6.5.

The DHM setup is based on a Mach–Zehnder interferometer. The light source SO is realized with three LEDs forming a RGB source with wavelengths 470, 530, and 630 nm. A liquid light guide LG (diameter of 3 mm) homogenizes the illumination. The light beam, collimated by L1, is filtered by the aperture P in order to increase the spatial coherence. The incoming light beam in the DHM is split by the beamsplitter BS1 into object and reference beams. The object beam, transmitted by BS1, illuminates the sample (SA) in transmission. The microscope lens (ML1) and lenses L3, L4, and L7 make the image of one plane of the sample on the CCD sensor. The back focal plane of L3, where a neutral density filter ND is located, is in the front focal plane of L4. The sensor is in the back focal plane of L7. The neutral density filter achieves a suitable beam ratio between the object and the reference beam.

The lenses ML1, L3, and L4 of the object beam have their equivalent counterparts in the reference path, respectively, the lenses ML2, L5, and L6, to achieve equivalent optical paths for the reference and object beams. In the reference path, there is an additional grating G and an optical stop S located, respectively, at the back focal planes of L5 and L6. The grating plane is conjugated with this sensor plane. In the front focal plane of the ML2 lens, an optical path compensator C is placed to roughly compensate for the optical thickness of the sample SA. One of the first diffraction orders created by the grating is not blocked by the optical stop and reaches the sensor plane with an incidence angle that allows the off-axis configuration [11]. The object and the reference beam paths are accurately adjusted by rotating the rotation assembly RA around an axis perpendicular to the optical axes.

As the grating G is conjugated to the sensor plane, we observe that the diffraction does not affect the alignment for spatial coherence superposition.

Let us now consider the partial temporal coherence influence on the fringe contrast. We assume first that the complex amplitude emerging out of the grating plane is

quasi-monochromatic of optical frequency . It is imaged on the sensor plane where it is expressed by:

$$g_o(x, y, \nu) = A \exp\left\{jk2\left(f_6 + f_7\right)\right\} \exp\left\{jKx\right\} g_i\left(-\frac{f_6}{f_7}x, -\frac{f_6}{f_7}x\right) s(\nu) \tag{6.1}$$

where g_o and g_i are, respectively, the complex amplitudes in the sensor plane and the back focal plane of the lens L6, is a constant, $k = 2\pi/\lambda$, f_6 and f_7 are the focal lengths of the lenses L6 and L7, K is the slant factor introduced by the grating on the incident beam on the sensor and $s(\nu)$ the spectral distribution. We consider now the partially temporal coherent illumination. To optimize the fringe contrast, the propagation times of the object and reference channels between BS1 and the sensor plane have to be equal as far as possible. The temporal behavior is obtained by considering the propagation of a Dirac optical pulse $\delta(t)$. For that purpose, we assume an infinitely broad constant spectrum and we compute the Fourier transformation of Eq. (6.1) on the frequency variable ν to obtain the temporal representation. Assuming that $s(\nu)$ is constant in the plane of g_i, it results in:

$$g_o(x, y, t) = A'\delta\left(t - \frac{2\left(f_6 + f_7\right)}{c}\right) \exp\left\{jKx\right\} g_i\left(-\frac{f_6}{f_7}x, -\frac{f_6}{f_7}x\right). \tag{6.2}$$

Equation (6.2) expresses that an optical Dirac pulse in the back focal plane of L6 takes an identical time $t = 2(f_6 + f_7)/c$, to reach every point of the sensor plane regardless of position, where c is the speed of light in the vacuum. Therefore, the grating does not introduce any disturbance to performing global path equalization between the reference and object beams in the off-axis configuration.

For the first color DHM tests, we used a monochromatic CCD camera. Therefore, we successively recorded the three holograms with the red, green, and blue LEDs switched on. The holograms are individually processed by the Fourier method to obtain, in the three colors, the complex amplitudes and the corresponding intensities and optical phases. Digital refocusing is achieved by using the reconstruction algorithm described in [1]. The color intensities are recombined to obtain a composite color image.

Figure 6.6 (Plate 10) shows results obtained on the alga *Odontella* sp., colored with neutral red dye. This figure shows the intensities of the recombined RGB channels for out of focus
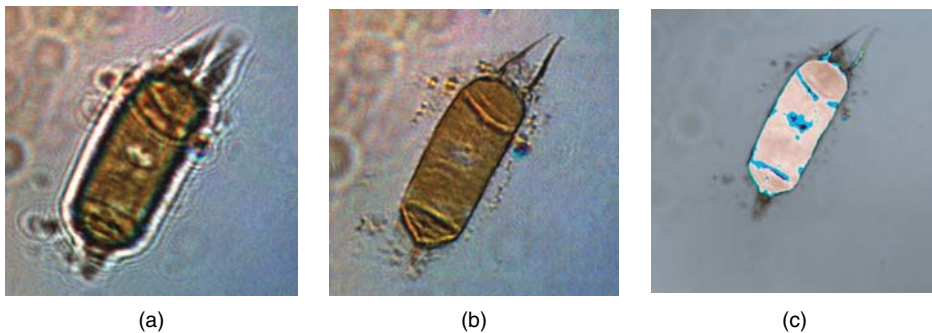

(a) (b) (c)

Figure 6.6 (Plate 10) (a) Out of focus color intensity of the alga *Odontella* sp., (b) refocused intensity, (c) composite phase image of the RGB channels. *See plate section for the color version*

recorded holograms (Fig. 6.6a), the refocused ones (Fig. 6.6b), and the combined phase image (Fig. 6.6c). The RGB LED source gives very low noise and the intensity of image quality is excellent and fully exploitable for microscopy purposes. We observed some small chromatic aberrations. There are small lateral shifts between the three chromatic channels and they are not simultaneously refocused. We measured a total drift of about 10 μm between the blue and red channels along the optical axis. To reduce those effects, we shifted laterally the three chromatic images and we applied slightly different digital holographic refocusing distances to simultaneously obtain the refocused RGB channel images.

6.3 Automated 3D Holographic Analysis

6.3.1 Extraction of the Full Interferometric Information

Once a digital hologram is recorded, the complex amplitude is first computed using the Fourier method [8,9]. The intensity and the phase are then computed. This process is illustrated in Fig. 6.7, where Fig. 6.7(a) represents a digital hologram of a green alga, *Pediastrium* sp. The computed intensity and phase information is illustrated respectively in Fig. 6.7(b) and (c). The non-uniform background present on the phase map is due to the experimental cell, which is not completely flat, and to small misalignment of the interferometer. Therefore it is necessary to implement a phase map correction that subtracts the background phase. A method based on the phase map derivative is developed and described in [12]. The resulting compensated phase map is illustrated in Fig. 6.8(a). Thanks to this aberration, compensation of the optical phase, the optical thickness of the alga is measured quantitatively. Figure 6.8(b) illustrates the pseudo-3D representation of this algae from which quantitative measurement can be performed.

6.3.2 Automated 3D Detection of Organisms

This part describes the methodology adopted to automatically detect all particles in the experimental volume, recently proposed in [13]. Holograms are first recorded at a frame rate of 24 frames per second with an exposure time of 200 μs. The recorded focus plane is set to the
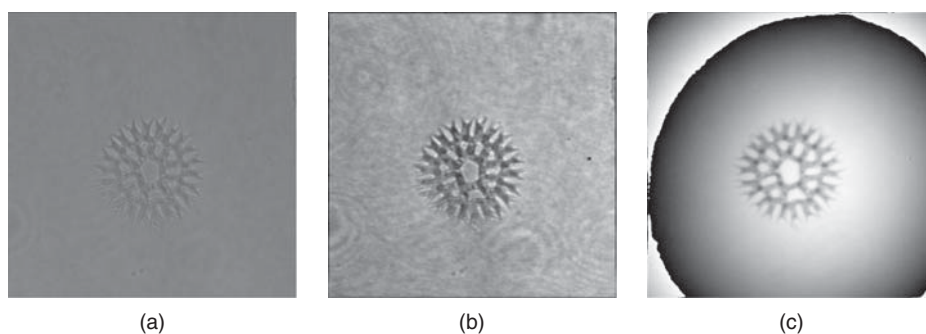

(a) (b) (c)

Figure 6.7 Extraction of the full interferometric information. (a) Recorded hologram of the alga *Pediastium* sp. (b) Intensity image. (c) Phase image

<div align="center">(a)   (b)</div>
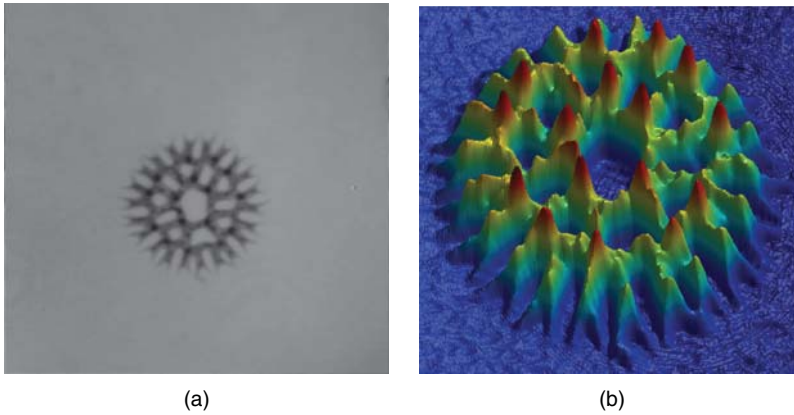
Figure 6.8   (a) Compensation of the phase. (b) Pseudo-3D representation of the algae (with inverted contrast)

middle of channel thickness. Once the full interferometric information is extracted from the digital holograms, automated 3D detection is performed.

The 3D detection of the particles is then split into two steps: (1) detection in the *X-Y* plane is performed, and (2) the position on the *Z*-axis is determined. *X* and *Y* are respectively the horizontal axis and the vertical axis, while the *Z*-axis is the depth axis. The determination of the *X-Y* position of particles can be done using a classical thresholding method based on a global threshold of the intensity or the compensated phase, depending on the species' nature. For large concentrations this method is not robust enough. Therefore a new approach based on propagating matrices has been investigated.

6.3.2.1   Using the Usual Thresholding Method

To detect the 3D position of each organism, a classical procedure consists in "thresholding" the intensity or the phase map depending on the nature of the objects under investigation. For opaque particles, the detection is made on the intensity image, while for transparent particles it is performed on the compensated phase images. The organisms under study in the frame of water quality project are algae and can be considered as phase objects. Therefore *X-Y* detection is achieved by analyzing the phase fluctuations with respect to the background values. The compensation of the phase images shifts the background close to the zero gray level. The particles are then detected by thresholding the compensated phase map to provide a rough detection of particles present in the *X-Y* plane field of view. This process uses the Otsu method [14] that chooses the threshold level to minimize the intra-class variance of the black and white pixels. The computation of the threshold is then used to convert the compensated phase into a binary image. The centroid of the segmented particle is then computed and a first set for the position in the *X-Y* plane is obtained. A filtering process is also implemented in order to remove all small particles that are not significant; for example, bacteria, dust, and other very small defects. The binary images are filtered by selecting the range of areas or sizes (major

and minor axis) of the particles of interest. The binary image is then cleaned and only contains the particles of interest.

Once the particle is detected in the *X-Y* plane, the *Z* position of the particle has to be determined. This position is established by numerically investigating the micro-channel volume (refocusing of the different slices). To determine the optimal focus plane, a refocusing criterion [15] whose robustness has been determined recently [16] is used. It has been shown that this refocusing criterion is maximal for phase objects as is the case with this experiment. The refocusing criterion is computed inside a region of interest (ROI) that is established around the detected particle [17]. This ROI is determined on the basis of the enlarged segmented area of each object in such a way that the diffraction patterns created by the object are also involved in the ROI.

When the *Z* position has been established, the particle is re-segmented in its focus plane to obtain a precise delimitation of the object. Indeed, the first segmentation (performed in the out of focus recorded plane) only provides a rough estimation of the size of the object. This first estimation is sufficient to determine the ROI for the *Z* scanning but cannot provide any precise information of the object for the classification. By segmenting in the focus plane, the precise shape and the *X-Y* position of the object can be computed, and thereby the 3D position of each object.

This method has been quantified by processing thousands holograms of different organisms, illustrated in Fig. 6.9. These three different organisms are typically present in water and were investigated for testing the detection software: cysts of the parasitic protozoan *Giardia lamblia*, as well as algae *Scenedesmus dimorphus*, and *Chlorella autotrophica*. The classification of these three organisms is presented in Section 6.4.

Applying the developed automated 3D detection algorithm, giving a mean detection score of 80.4% (standard deviation: 5.2%). This mean rate has been computed by comparing a manual and an automated count. This score is not high enough and can be explained by the fact that the detection is based on a simple global thresholding of the compensated phase in the recorded plane. For large concentrations, organisms can be recorded with very different focus depths and thus can lead to different optical phase fluctuations inside the same phase image. All particles then cannot be detected with the same threshold. In Fig. 6.10, an example of concentrated *Chlorella autotrophica* samples are shown where we can see in Fig. 6.10(b) some
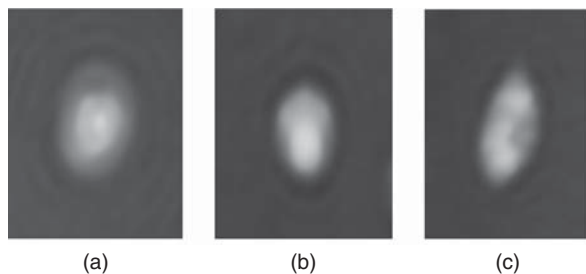

(a)   (b)   (c)

Figure 6.9   Cropped studied organisms: Compensated phase images (a) *Giardia lamblia*, (b) *Chlorella autotrophica*, (c) *Scenedesmus dimorphus*. *Source*: A. El Mallahi, C. Minetti and F. Dubois 2013. Reproduced with permission from the Optical Society
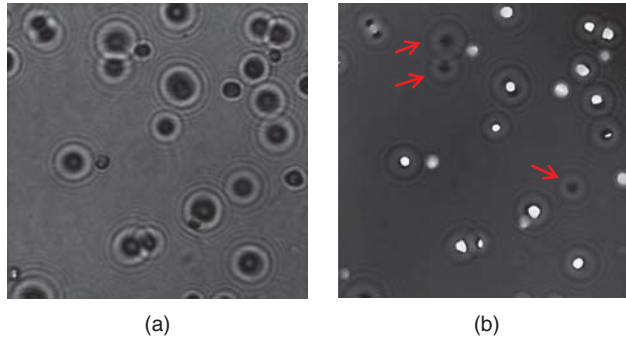
Figure 6.10   (a) Intensity image of an algae *Chlorella autotrophica*. (b) Compensated phase map where we can see that some algae (with the arrows) cannot be detected because they are far from the recorded plane. *Source*: A. El Mallahi, C. Minetti and F. Dubois 2013. Reproduced with permission from the Optical Society

algae (with arrows) that will not be detected by a global threshold. Therefore, a new procedure based on the propagation operator has been investigated to overcome this limitation.

6.3.2.2   Using Robust Propagating Matrices

In the case of large concentrations, the previous more usual method is not robust enough to detect particles in the volume with a detection level higher than 80%. Therefore, a new robust method for the 3D automated detection based on the free propagation operator is investigated.

Let us consider the complex amplitude distribution $u_d(x', y')$ refocused at a distance d along the optical axis by computing the Kirchhoff–Fresnel propagation integral in the paraxial approximation:

$$u_d\left(x', y'\right) = \exp\left(jkd\right) F_{x',y'}^{-1} \exp\left(\frac{-jkd\lambda^2}{2}\left(v_x^2 + v_y^2\right)\right) F_{v_x,v_y}^{+1} u_0\left(x, y\right) \qquad (6.3)$$

where $u_0(x, y)$ is the complex optical field in the focus plane, $u_d(x', y')$ is the complex amplitude field propagated at a distance d along the optical axis, $k = 2\pi/\lambda$, (x, y) and (x', y') are the spatial variables respectively in the focus plane and in the reconstructed plane, (v_x, v_y) are the spatial frequencies, $j = \sqrt{-1}$ and $F^{\pm 1}$ denotes the direct and inverse 2D continuous Fourier transformations. The Eq. (6.3) is implemented in a discrete form:

$$u_d(s'\Delta, t'\Delta) = \exp(jkd) F_{s',t'}^{-1} \exp\left(\frac{-jkd\lambda^2}{2N^2\Delta^2}\left(U^2 + V^2\right)\right) F_{U^2,V^2}^{+1} u_0(s\Delta, t\Delta) \qquad (6.4)$$

where N is the number of pixels in both directions (to match the Fast Fourier transform computations), s, t, s', t', U, and V are integers varying from 0 to $N - 1$, and $F^{\pm 1}$ is now the direct and inverse discrete Fourier transformations.

The complex amplitude $u_d(s'\Delta, t'\Delta)$ is computed for each refocused distance d inside the experimental volume, from the lower to the upper slides of the micro-channel. Then we

compute two 3D matrices containing respectively the intensity I and the optical phase P for all the refocused distances:

$$I\left(s'\Delta, t'\Delta, d\right) = \text{Re}\left(u_d\left(s'\Delta, t'\Delta\right)\right)^2 + \text{Im}\left(u_d\left(s'\Delta, t'\Delta\right)\right)^2$$

$$P\left(s'\Delta, t'\Delta, d\right) = \tan^{-1}\left(\frac{\text{Im}\left(u_d\left(s'\Delta, t'\Delta\right)\right)}{\text{Re}\left(u_d\left(s'\Delta, t'\Delta\right)\right)}\right) \tag{6.5}$$

where Re and Im are respectively the real and imaginary parts. Note here that each plane corresponding to a distance d of the 3D P-matrix can be compensated for, as described in this section, in order to remove the background.

Four matrices can now be computed for respectively the minimum and the maximum along the d dimension of the 3D matrices I and P. For these two 3D matrices, we investigate all the d planes and we keep the minimum and the maximum; giving four new matrices:

$$I_{\min}\left(s'\Delta, t'\Delta\right) = \min_d\left(I\left(s'\Delta, t'\Delta, d\right)\right)$$

$$I_{\max}\left(s'\Delta, t'\Delta\right) = \max_d\left(I\left(s'\Delta, t'\Delta, d\right)\right)$$

$$P_{\min}\left(s'\Delta, t'\Delta\right) = \min_d\left(P\left(s'\Delta, t'\Delta, d\right)\right)$$

$$P_{\max}\left(s'\Delta, t'\Delta\right) = \max_d\left(P\left(s'\Delta, t'\Delta, d\right)\right) \tag{6.6}$$

where $\min_d$ and $\max_d$ are, respectively, the minimum and the maximum along all d planes. It results in four bi-dimensional matrices that can be used simultaneously for the 3D detection of particles. Fig. 6.11(a−d) illustrates the four matrices of Eq. (6.6) based on the intensity and phase image in Fig. 6.10.

Each of these four matrices can then be automatically thresholded using the Otsu method, providing four thresholding parameters, $T_{I_{\min}}, T_{I_{\max}}, T_{P_{\min}}$, and $T_{P_{\max}}$. On the basis of the four thresholded images, a simple logical operation (logical AND) provides the binary matrix Fig. 6.11(e) and robust 2D detection becomes possible. The scanning along the z-axis is performed to detect the z position of each detected particle as described in the previous section.

Applying the same methodology as in the previous section, the mean detection rate now gives 95.1% (standard deviation: 2.3%) of correct detections thanks to the propagation operator that easily detects out-of-focus objects. This score obviously depends on the sample nature. Indeed, samples with a lot of aggregates or clogging organisms can perturb the detection rate. To overcome this limitation, a new method, based on a complete analysis of the evolution of the focus planes, has been recently developed to separate aggregates of overlapped particles [18].

6.4   Applications

The developed automated 3D detection process has been used for different applications. We present two of them here. The first one is dedicated to the classification of micro-organisms while the second one looks at the dynamics of red blood cells.
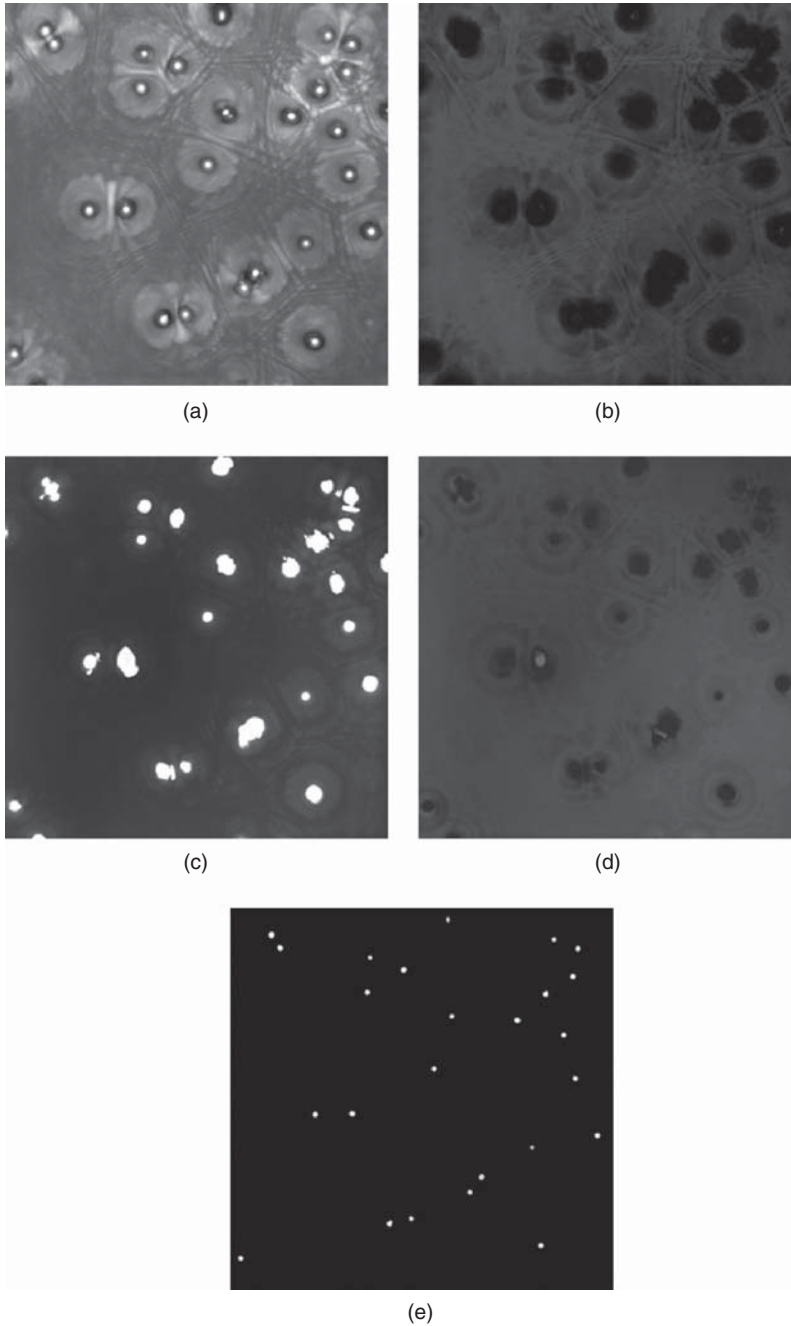
(a)

(b)

(c)

(d)

(e)

Figure 6.11 Propagating matrices (a) I_{max}, (b) I_{min}, (c) P_{max} (+ compensation), (d) P_{min} (+ compensation), (e) by thresholding these four matrices and then combining them, a binary matrix can be computed, on which robust 2D detection can be done. *Source*: A. El Mallahi, C. Minetti and F. Dubois 2013. Reproduced with permission from the Optical Society

6.4.1 *Holographic Classification of Micro-Organisms*

Object classification by digital holography is a promising approach offering a large number of applications. The development of automated procedures to detect and recognize living organisms using digital holography are of significant benefit. Using single-exposure on-line holographic microscope (SEOL), Javidi *et al*. have investigated 3D imaging and recognition of micro-organisms in [19–22] where the Fresnel field of the object illuminated by coherent light is recorded. In [23], 3D phase objects (triangle, rectangle, and circle) have been also recognized and classified by digital Fresnel holography. The identification of microorganisms has been addressed in [24] by the use of microscopic integral imaging. It is based on recording the multi-view directional information of a 3D scene with incoherent illumination. Another class of pattern recognition problem based on photon counting imagery has been investigated in [25], where the effect of noise has been taken into account to recognize a target in a 3D scene. Recently in [26], Liu *et al*. have applied statistical clustering algorithms to recognize and classify two classes of red blood cells (RBCs). Also recently, an automated statistical procedure to quantify the morphology of RBCs using DHM was presented in [27].

We have developed a classification procedure based on the full interferometric information of species (intensity + phase). For this reason, it makes sense to use the term *holographic classification*. This procedure has been applied to several applications. One of them concerns the monitoring of drinking water resources. Over the past three decades, serious health crises associated with the parasitic protozoan *Giardia lamblia* have triggered major efforts worldwide for its detection in the water resources used to produce drinking water [28,29]. This flagellated protozoan is responsible for giardiasis [30], a widespread diarrheal disease affecting around two hundred million symptomatic individuals in the world [28]. Humans can be infected through the following transmission routes: person-to-person transmission, direct contact with contaminated mammals, or ingestion of infected food and/or water. *Giardia lamblia* is able to live in very harsh environments thanks to its vegetative transmission form, the cyst, whose size varies between 11–14 μm in length and 6–10 μm in width. In particular, the cyst is able to resist the levels of chlorine traditionally used in water disinfection. Considering the lack of efficient preventive means against *Giardia* cysts, they must be detected as early as possible in water resources [31]. Usual detection methods are too time consuming as they require the use of different stains prior to detection and recognition.

A new classification procedure has been developed and applied to the monitoring of drinking water. Three different organisms (typically present in water) were investigated in this study: cysts of *Giardia lamblia*, as well as the algae *Scenedesmus dimorphus*, and *Chlorella autotrophica*. *Giardia lamblia* is a parasitic flagellated protozoan that was obtained in cyst form. *Scenedesmus dimorphus* and *Chlorella autotrophica* are both types of green algae and were selected for their high similarities in size range and shape to *Giardia lamblia* cysts [32].

These three species are illustrated in Fig. 6.9. A three-class classification is then investigated. Once the 3D position of each particle is detected, a set of features is computed to perform their classification. Two types of feature can be extracted from holographic information. In the first step, a set of morphological features can be obtained from the segmentation of the compensated phase image. In the second step, as both intensity and optical phase are extracted from holograms, textural features based on these two physical quantities are computed.

6.4.1.1 Using Morphological Features

A set of classical morphological features can be first extracted from the segmented binary image of the detected organisms. This set of region descriptors includes the following: *area*, *perimeter*, *major* and *minor axes*, *eccentricity*, and *equivalent circle diameter*. Area is calculated as the number of pixels in the segmented region, the perimeter is the number of pixels in the boundary of the segmented particles. The major and minor axes are the length in pixels of the major and minor axes of the ellipse. Eccentricity is computed as the ratio of the distance between the foci of the ellipse surrounding the segmented particle and its major axis length. The value of the feature is between 0 and 1 (an ellipse whose eccentricity is 0 is a circle, while an ellipse whose eccentricity is 1 is a line segment). The *equivalent circle diameter* is a number specifying the diameter of a circle with the same area as the region. Each value is then converted into μm, given by the field of view (FOV) of the camera and the magnification of the objective lenses used (63× objective lenses, given a FOV of 115 × 115 μm).

To perform a classification process, the best discriminants among this set of morphological features have to be determined. As the three species have very similar shapes and sizes, this list of features is not sufficient. Moreover, during the particle's travel in the micro-channel, it can rotate around its own axis and any of these out-of-plane orientations can be recorded on the holograms. It results in a wide range of different morphological values that can be captured for organisms of the same species.

Consequently, in our multi-species classification experiment, the use of those morphological features only would lead to substantial regions of overlap among similar species in the feature space. Those features are, therefore, not sufficient to adequately distinguish between species used in our experiments. For a robust classification, other features have to be introduced and added to the morphological features. Given the advantage of capturing both intensity as well as phase information with digital holographic microscopy, we choose to introduce textural features to the classification procedure. As we use the full interferometric information, the term *holographic classification* is used.

6.4.1.2 Using Textural Features

Digital holography gives information about both the intensity and phase of the object. When an object is focused, the intensity gives information about the absorbance of the organism while the phase is a measure of the optical thickness.

Thanks to these two physical quantities, a textural analysis based on statistical measures can be computed. A typical category of such measures is based on statistical moments whose expression of the *n*th is given by:

$$\mu_n = \sum_{i=0}^{L-1} (q_i - m)^n p(q_i) \tag{6.7}$$

where q_i is the intensity, $p(q)$ is the histogram of the intensity levels in a region, L is the number of possible intensity levels (in this case for gray level images, $L = 256$) and $m = \sum_{i=0}^{L-1} q_i p(q_i)$ is the mean intensity.

These measures are based on the histogram of the pixel intensity value. For each image, a set of six texture measures is computed, which are: *average gray level* and *average contrast*, *smoothness*, *skewness*, *uniformity*, and *entropy*. The mathematical expression of those six measures can be found in [33]. All these textural features are measured in the domain given by the segmentation of the particle. The first two features, average gray level and average contrast, give the mean values in a gray level scale with its standard deviation. The smoothness (R) is measured inside each particle domain and is dependent on the variance (which is normalized to the range [0, 1] by dividing it by $(L-1)^2$). The smoothness equals 0 for the region of constant intensity and increases with fluctuations in pixel value. It ranges from $0-1$. The third statistical moment measures the skewness of the histogram. It gives 0 for symmetric histograms, a positive value for histograms skewed to the right above the mean and negative value for histograms skewed to the left. This moment is also normalized to 1 by dividing it by $(L-1)^2$. The uniformity texture measure is at its maximum when all gray levels are equal. The entropy of the object region is also implemented to quantify the randomness of the texture.

These six texture features are computed for all detected organisms both on the intensity and the compensated phase images. A set of 12 textural features is then available for each organism to be classified. Figure 6.12 shows the pseudo-3D representation of the compensated phase of organisms illustrated in Fig. 6.9. We can see that even if there is a high similarity between the different species, thanks to the optical phase it becomes possible to distinguish and discriminate between them. Indeed, in spite of having the same shapes, these organisms have different optical thicknesses that are exploited thanks to the interferometric information. Figure 6.13 (Plate 11) illustrates two feature spaces, one using textural features based on intensity information (Fig. 6.13a) and the other using textural features based on compensated phase information (Fig. 6.13b). We observe that the use of quantitative optical phase information can lead to high separability between the three species. It has to be pointed out that the use of a partially coherent source provides phase maps of high quality with a very low noise level [34] permitting an accurate textural analysis.

6.4.1.3 Robust SVMs Classifier

After a graphic analysis of the dataset, a classification process is performed. For this, support vector machines (SVMs) [35–37] are investigated to optimally separate the dataset into the three categories. The basic idea of this supervised learning model is the construction of a set of $(N-1)$-dimensional hyperplanes (N = number of features = 18 in our case) that optimally separates the data classes in the N-dimensional feature space. For each hyperplane, the best separation is obtained by the hyperplane that has the largest distance to the nearest training data point of any class. The multi-class classification is performed by training one SVM per class using a one-against-all method [38]. The use of a radial basis function (RBF) kernel is chosen as a majority of features can be separated by a nonlinear region. This kernel function maps the data into a different space where the hyperplanes can be used to separate between classes. The parameters of the SVMs (a cost parameter that controls the flexibility of the hyperplanes to avoid overfitting and the parameter of the RBF kernel) are automatically selected based on a grid search. The evaluation is performed by a 10-fold cross-validation. The dataset is randomly partitioned into 10 subsets, performing the training on nine subsets (training set), and validating
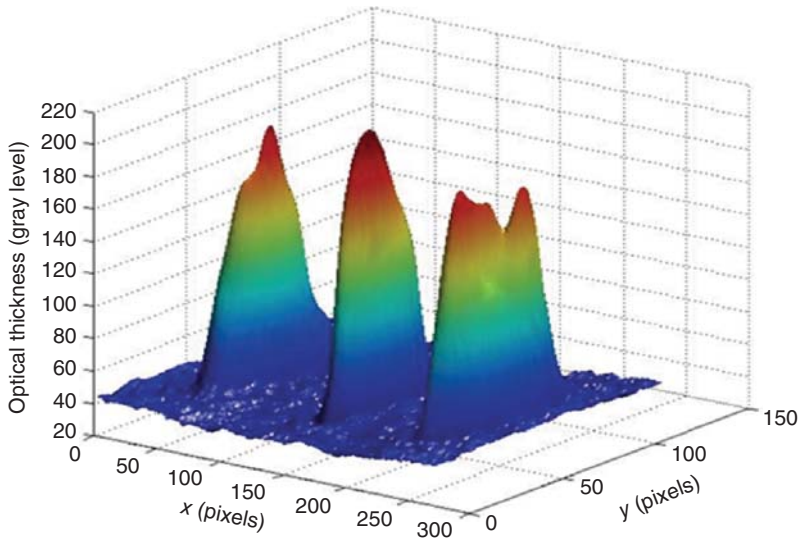
Figure 6.12 Pseudo-3D representation of the compensated phase of the organisms illustrated in Fig. 6.9, where we can see that, even if the three organisms have the similar morphology features, thanks to the optical phase, it becomes possible to distinguish between them. Textural features are therefore selected to perform the classification process rather than morphological ones. The *z*-axis is the optical thickness. *Source*: A. El Mallahi, C. Minetti and F. Dubois 2013. Reproduced with permission from the Optical Society
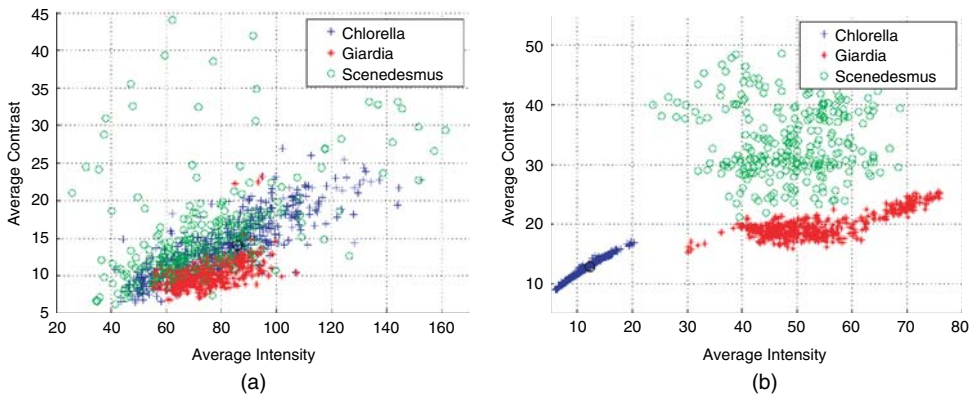

Figure 6.13 (Plate 11) Feature space representation using (a) intensity information of the detected particles of the three species, and (b) compensated phase of detected particles of the three species *See plate section for the color version*

Table 6.1   Performance of the classifier (%) with the corresponding standard deviation: Confusion matrix to compare the truth labels and the decisions of the classifier

Actual Classes	Predicted Classes		
	Chlorella	Giardia	Scenedesmus
Chlorella	**98.1 ± 2.3**	1.1 ± 0.2	0.8 ± 0.3
Giardia	0.8 ± 0.2	**98.6 ± 1.7**	0.6 ± 0.1
Scenedesmus	1.1 ± 0.5	1.4 ± 0.4	**97.5 ± 2.4**

the classifier on the last subset (testing set). The cross validation is then repeated 10 times, with each of the 10 subsets used only once as the testing set. The 10 results are then averaged to produce a single robust mean estimation, with its corresponding standard deviation.

In Table 6.1, the confusion matrix of the classifier is shown to illustrate the performance of the algorithm. It contains information about the actual and predicted classification of the three tested species. The diagonal of the confusion matrix stores the number of correctly classified organisms, while the non-diagonal elements refer to the misclassified objects. Thanks to the complete list of features (morphological and textural) resulting from the full interferometric information, a robust classifier that distinguishes the three species with more than 97% is built. (There are approximately 500 samples of each class.) For the *Giardia lamblia* cysts, the proportion of organisms that were correctly identified is 98.6% while 0.8% of all the detected *Giardia* has been classified as *Chlorella autotrophica* alga and 0.6% as *Scenedesmus dimorphus* alga. The accuracy of the built classifier can be computed as the total number of correct predictions and gives a level of 98.1%.

6.4.2   Dynamics of Red Blood Cells (RBCs)

Blood is a complex biological fluid made up of more than 50% with red blood cells (RBC). Those cells, with a disk diameter of approximately 6.2–8.2 μm, a thickness at the thickest point of 2–2.5 μm, and a minimum thickness in the center of 0.8–1 μm, are much smaller than most other human cells. They are deformable and can adopt various shapes depending on the channel they are flowing in. They are the principal means of delivering oxygen to body tissues via blood flow through the circulatory system. They take up oxygen in the lungs or gills and release it while squeezing through the body's capillaries. These cells' cytoplasm is rich in hemoglobin, an iron-containing biomolecule that can bind to oxygen and is responsible for blood's red color.

The distribution of RBCs in a confined flow is inhomogeneous and shows a marked depletion near the walls, due to competition between migration away from the walls and shear-induced diffusion resulting from interactions between particles [39].

The migration of blood cells forms the physical basis of the formation of a cell free plasma layer near vessel walls in the microcirculation. Furthermore, with the very high concentration of RBCs in human blood, strong hydrodynamic interactions take place. Consequently, blood is a complex flow from a rheological point of view leading to complex flow patterns in micro-circulation networks where the diameter of blood vessels becomes comparable to the cell size.

Those inhomogeneities have important consequences on the transport of oxygen and may lead to situations where one branch of a capillary bifurcation is not irrigated by RBCs.

In this part, we report the investigation and quantification of the lift force that pushes cells away from the vessel walls when a shear flow is applied. To cope with the DHM requirements in terms of concentration and limit the hydrodynamic interactions between pairs of cells, we work with highly diluted and washed blood. The resulting fluid is made of RBCs in an external solution (BSA – bovine serum albumin and PBS – phosphate buffer saline) alone or in combination with Dextran (typically 1%). With the addition of Dextran, one can increase the viscosity of the external fluid, and easily play on lift velocity. To avoid any screening of the lift by sedimentation, we perform these experiments in microgravity during parabolic flight campaigns onboard the Airbus A300 Zero-G from Novespace.

6.4.2.1   Experimental Protocol

Experiments are performed in a shear flow chamber made of two glass plates with a gap of about 170 μm (see Fig. 6.14). The bottom plate is fixed while the top one rotates creating a linear velocity profile of the fluid inside the chamber. The suspension of RBCs is inserted via the inlet in the center of the bottom plate and the DHM monitors the suspension at a distance of 7 cm with respect to the center of the cell.

During a parabolic maneuver creating a period of 22 s of microgravity (10^{-2} g), we first undergo a hyper gravity period of 1.8 g. We take the benefit of this period to stop the shear flow and let the cells sediment on the bottom plate of the cell. When entering the microgravity period, the shear flow is applied and the DHM monitors the 22 s period of microgravity. The RBC, initially lying on the bottom plate will lift away from the wall and the 3D position of
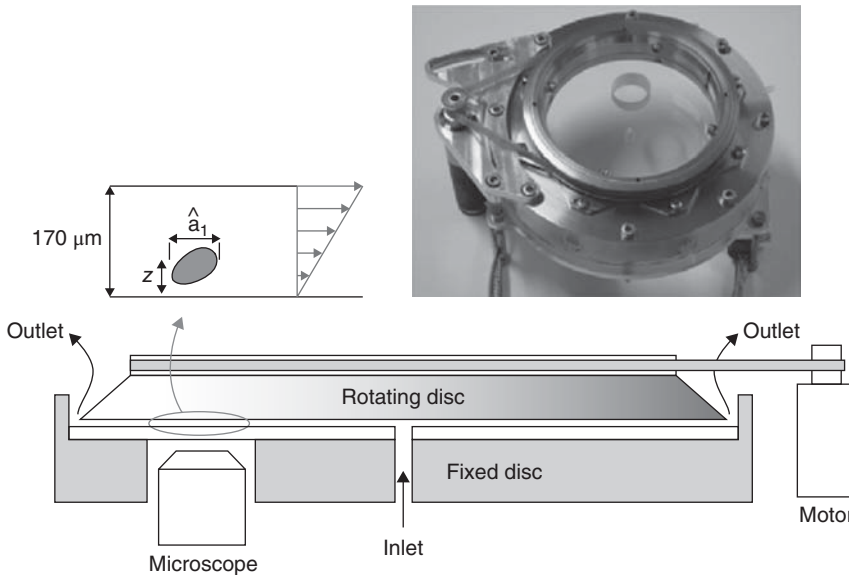

Figure 6.14   Shear flow chamber used in parabolic flights

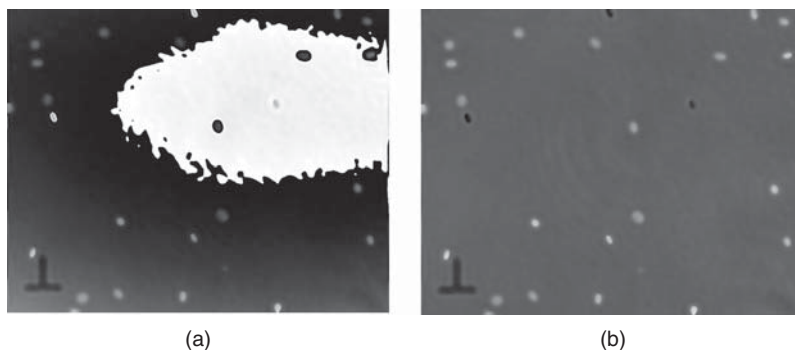(a)   (b)

Figure 6.15   (a) Example of phase maps with RBCs, and (b) compensated phase image

each RBC will be retrieved thanks to the interferometric information obtained with the DHM. This zero-g period is then followed by another 1.8 g period where the shear flow is stopped again to let the sample sediment. In this way, we have a very simple and reproducible initial condition.

6.4.2.2   Hologram Analysis

Holograms are acquired at a frequency of 24 holograms per second. The field of view is $270 \times 215\,\mu m$. Depending on the concentration of the sample, between 10 and 100 cells are present in the field of view. Thanks to an adequate adjustment of the interferometer, we obtain very flat phase maps that can easily be compensated [12] resulting in bright spots (RBC) on an almost constant background (see Fig. 6.15). The *X-Y* detection of the cells is made on a simple threshold of the compensated phase map. When the refractive index difference between cells and the external solution is not sufficient to detect the *X-Y* position with a simple threshold, we use the propagation matrices (described earlier) that give more robust and reliable results.

Thanks to the mono dispersed size of RBCs, we determine the $\underline{Z}$ position by locally propagating around the *X-Y* position of each RBC with a fixed region of interest (ROI) of 120×120 pixels. Red blood cells behave like phase objects but have a non-negligible absorption. They cannot be considered either as pure phase objects or as pure amplitude objects. Consequentially, the best focus is determined by propagating the ROI along the different *Z* values and by computing, for each plane, the integrated gradient inside the ROI. The curve exhibits a well-defined and narrow minimum at the best focus plane of the object. This procedure is repeated for each RBC inside each hologram and provides the evolution of the suspension as a function of time.

6.4.2.3   Experimental Results

The lift force of deformable objects has been subject to a theoretical study by Olla [40,41] and a predictive law has been determined, which gives the distance from object to wall as a function of the shear rate (γ), the radius of the object (R), the time (t), and a parameter (U) describing the lift velocity and containing the viscosity ratio (between inner and outer fluid).
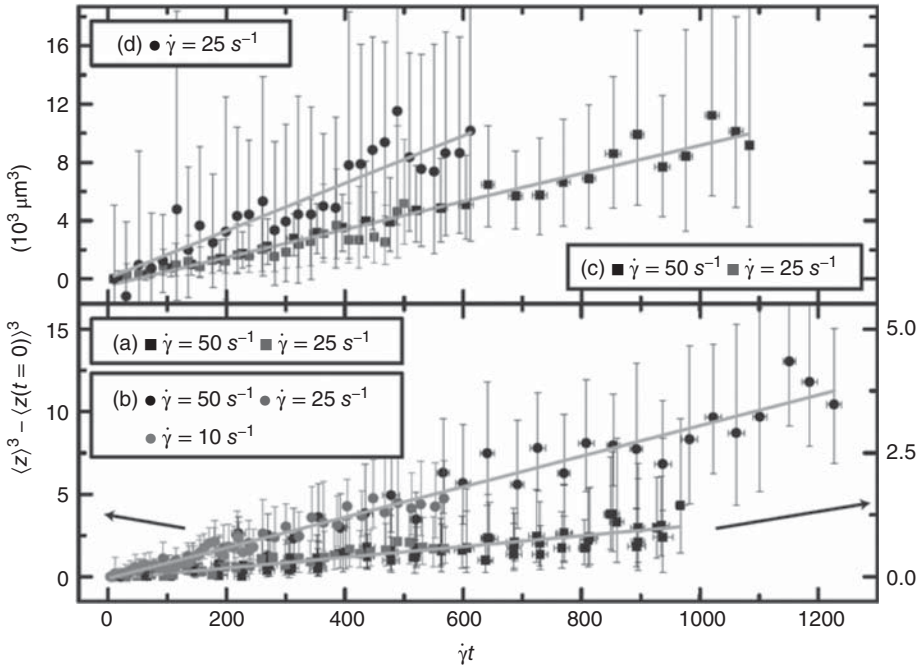
Figure 6.16   RBC: wall distance $<z^3>$ vs. γt for different outer viscosities: (a) 1.4 mPa.s; (b) 6.1 mPa.s; (c) 9.3 mPa.s; (d) 13 mPa.s. Bold lines indicate fit to Olla's prediction, with $UR^3 = 0.36, 3.1, 3.2, 5.4\,\mu m^3$, respectively. *Source*: G. Coupier, A. Srivastav, C. Minetti, and T. Podgorski 2013. Reproduced with permission from the American Physical Society

The law can be reduced to the following expression:

$$\frac{\langle Z^3 \rangle}{R^3} = 3U\gamma t \tag{6.8}$$

exhibiting a linear dependency between the rescaled mean position of objects to the power of 3 and the shear rate multiplied by time. Experimental results confirm this predictive law very well by exhibiting linear curves with different lift velocities for the different viscosity ratios (Fig. 6.16). By symmetry, a tumbling rigid object should not migrate on average. The non-zero lift suggests that RBC deformability allows symmetry breaking: It is stretched when oriented in the direction of the elongational component of the flow, while it is compressed when orthogonal, resulting in an averaged asymmetric shape, leading to a migration law similar to the one known for a fixed shape and orientation. By increasing the external viscosity, the stresses on the RBC membrane are higher and lead to increased deformation, which in turn enhances the lift.

   These results clearly demonstrate the capability of digital holographic microscopy for monitoring RBC suspension in micro-flow circulation.

6.5   Conclusion

In this chapter we showed developments on DHM working with partially coherent illumination that allows us to drastically reduce coherence noise. The several described instruments

have their specific advantages with respect to the applications. In this way, it is possible to achieve high quality phase shifting or off-axis DHMs. More recently, we proposed the implementation of a color off-axis DHM making possible the use of weak spatial and temporal coherences sources. The improved image quality leads to the implementation of powerful processing up to the automated classification of living organisms. With respect to the classification, the additional phase information constitutes a huge improvement. The DHMs working with partial coherence sources are demonstrated on applications that are currently developed in our laboratory.

Acknowledgments

References

[1] Dubois, F., Joannes, L., and Legros, J.C., "Improved three-dimensional imaging with a digital holography microscope with a source of partial spatial coherence," *Appl. Optics*, **38**, 7085–7094 (1999).

[2] Zhang, T., and Yamaguchi, I., "Three-dimensional microscopy with phase-shifting digital holography," *Opt. Lett.* **23**, 1221–1223 (1998).

[3] Dubois, F., Yourassowsky, C., and Monnom, O., "Microscopie en holographie digitale avec une source partiellement cohérente," in *Imagerie et Photonique pour les Sciences du Vivant et la Médecine*, M. Faupel, P. Smigielski, and R. Grzymala, (eds) Fontis Media (2004).

[4] Marquet, P., Rappaz, B.J., Magistretti, P.J., Cuche, E., Emery, Y., Colomb, T., and Depeursinge, C., "Digital holographic microscopy: a noninvasive contrast imaging technique allowing quantitative visualization of living cells with subwavelength axial accuracy," *Opt. Lett.* **30**, 468–470 (2005).

[5] Dubois, F., Yourassowsky, C., Monnom, O., Legros J.C., Debeir, O., Van Ham, P., *et al.*, "Digital holographic microscopy for the three-dimensional dynamic analysis of in vitro cancer cell migration," *J. Biomed. Opt.* **11–5**, 054032 (2006).

[6] Carl D., Kemper B., Wernicke, G., and von Bally, G., "Parameter-optimized digital holographic microscope for high-resolution living-cell analysis," *Appl. Opt.* **43**, 6536–6544 (2004).

[7] Dubois, F., N. Callens, C. Yourassowsky, M. Hoyos, P. Kurowski and O. Monnom, "Digital holographic microscopy with reduced spatial coherence for 3D particle flow analysis," *Applied Optics*, **45**, No. 5, 964–961 (2006).

[8] Kreis, T., "Digital holographic interference-phase measurement using the Fourier-transform method," *J. Opt. Soc. Am. A* **3**, 847–855 (1986).

[9] Takeda, M., Ina, H., and Kobayashi, S., "Fourier-transform method of fringe-pattern analysis for computer-based topography and interferometry," *J. Opt. Soc. Am.* **72**, 156–160 (1982).

[10] Dubois, F. and Yourassowsky, C., "Full off-axis red-green-blue digital holographic microscope with LED illumination," *Optics Letters* **37**(12), 2190–2192 (2012).

[11] Kolman, P. and Chmelík, R., "Coherence-controlled holographic microscope", *Opt. Express* **18**, 21990–22003 (2010).

[12] Minetti, C., Callens, N., Coupier, G., Podgorski, T., and Dubois, F., "Fast measurements of concentration profiles inside deformable objects in microflows with reduced spatial coherence digital holography," *Appl. Op.* **47**, 5305–5314 (2008).

[13] El Mallahi, A., Minetti, C., and Dubois, F., "Automated three-dimensional detection and classification of living organisms using digital holographic microscopy with partial spatial coherent source: application to the monitoring of drinking water resources," *Appl. Optics* **52**, A62–A80 (2013).

[14] Sezgin, M. and Sankur, B., "Survey over image thresholding techniques and quantitative performance evaluation," *Journal of Electronic Imaging* **13**(1), 146–165 (2004).

[15] Dubois, F., Schockaert, C., Callens, N., and Yourassowsky, C., "Focus plane detection criteria in digital holography microscopy by amplitude analysis," *Opt. Exp.* **14**, 5895–5908 (2006).

[16] El Mallahi, A. and Dubois, F., "Dependency and precision of the refocusing criterion based on amplitude analysis in digital holographic microscopy," *Opt. Exp.* **19**, 6684–6698 (2011).

[17] Antkowiak, M., Callens, N., Yourassowski, C. and Dubois, F., "Extended focusing imaging of a microparticle field with digital holographic microscope," *Opt. Exp.* **33**, 1626–1628 (2008).

[18] El Mallahi, A. and Dubois, F., "Separation of overlapped particles in digital holographic microscopy," *Opt. Exp.* **21**, 6466–6479 (2013).

[19] Javidi B., Moon, I., Yeom, S., and Carapezz, E., "Three-dimensional imaging and recognition of microorganisms using single-exposure on-line (SEOL) digital holography," *Opt. Exp.* **13**, 4492–4506 (2005).

[20] Stern, A. and Javidi, B., "Theoretical analysis of three-dimensional imaging and recognition of micro-organisms with a single-exposure on-line holographic microscope," *J. Opt. Soc. Am. A* **24**, 163–168 (2007).

[21] Moon, I. and Javidi, B., "Shape tolerant three-dimensional recognition of biological microorganisms using digital holography," *Opt. Exp.* **13**, 9612–9622 (2005).

[22] Javidi, B., Yeom, S., Moon, I., and DaneshPanah, M., "Real-time automated 3D sensing, detection, and recognition of dynamic biological micro-organic events," *Opt. Exp.* **14**, 3806–3826 (2006).

[23] Nelleri, A., Joseph, J., and Singh, K., "Recognition and classification of three-dimensional phase objects by digital Fresnel holography," *Appl. Opt.* **45**, 4046–4053 (2006).

[24] Javidi, B., Moon, I., and Yeom, S., "Three-dimensional identification of biological microorganism using integral imaging," *Opt. Exp.* **14**, 12096–12108 (2006).

[25] DaneshPanah, M., Javidi, B., and Watsin, E.A., "Three dimensional object recognition with photon counting imagery in the presence of noise," *Opt. Exp.* **18**, 26450–26460 (2010).

[26] Liu, R., Dey, D.K., Boss, D., Marquet, O., and Javidi, B., "Recognition and classification of red blood cells using digital holographic microscopy and data clustering with discriminant analysis," *J. Opt. Soc. Am. A* **28**, 1204–1210 (2011).

[27] Moon, I., Javidi, B., Yi, F., Boss, D., and Marquet, P., "Automated statistical quantification of three-dimensional morphology and mean corpuscular hemoglobin of multiple red blood cells," *Opt. Exp.* **20**, 10295–10309 (2012).

[28] World Health Organization (WHO), "Guidelines for drinking-water quality Volume 1 Recommendations," Geneva (2006).

[29] Huang, D.B. and White, A.C., "An updated review on Cryptosporidium and Giardia," *Gastroenterol. Clin. N. Am.* **35**, 291–314 (2006).

[30] Craun, G.F., "Waterborne giardiasis," *Human Parasitic Diseases* **3**, 267–293 (1990).

[31] Bouzid, M., Steverding, D., and Tyler, K.M., "Detection and surveillance of waterborne protozoan parasites," *Cur. Opin. Biotechnol.* **19**, 302–306 (2008).

[32] Rodgers, M.R., Flanigan, D.J., and Jakubowski, W., "Identification of algae which interfere with the detection of *Giardia* cysts and *Cryptosporidium* oocysts and a method for alleviating this interference," *Appl. Environ. Microbio.* **61**, 3759–3763 (1995).

[33] Gonzalez, R.C. and Woods, R.E., *Digital Image Processing*, Prentice Hall, Upper Saddle River, NY (2002).

[34] Dubois, F., Novella Requena, M.-L., Minetti, C., Monnom, O., and Istasse, E., "Partial coherence effects in digital holographic microscopy with a laser source," *Appl. Opt.* **43**, 1131–1139 (2004).

[35] Cortes, C. and Vapnik, V., "Support vector network," *Machine Learning* **20**, 273–297 (1995).

[36] van der Heijden, F., Duin, R.P.W., de Ridder, D., and Tax, D.M.L., *Classification*, Parameter Estimation and State Estimation, John Wiley & Sons, Ltd, Chichester (2004).

[37] Webb, A., *Statistical Pattern Recognition*, John Wiley & Sons, Ltd, Chichester (2002).

[38] Chang, C.-C. and Lin, C.-J., "LIBSVM: A library for support vector machines," *ACM Trans. Intell. Syst. Technol.* **2**, 1–27 (2011).

[39] Grandchamp, X., Coupier, G., Srivastav, A., Minetti, C., and Podgorski, T., "Lift and down-gradient shear-induced diffusion in red blood cell suspensions," *Phys. Rev. Lett.* **110**, 108101 (2013).

[40] Olla P., "The lift on a tank-treading ellipsoidal cell in a shear flow," *J. Phys. II*, **7**, 1533 (1997).

[41] Callens, N., Minetti, C., Coupier, G., Mader, M., Dubois, F., Misbah, C., and Podgorski, T., "Hydrodynamic lift of vesicles under shear flow in microgravity," *Europhys. Lett.* **83**(2), 24002 (2008).